High-Resolution Recognition of Orbital Angular Momentum Modes in Asymmetric Bessel Beams Assisted by Deep Learning

Pengfei Xu(徐鹏飞), Xin Tong(童鑫), Zishuai Zeng(曾子帅),
Shuxi Liu(刘书悉), and Daomu Zhao(赵道木)*

Zhejiang Key Laboratory of Micro-nano Quantum Chips and Quantum Control, School of Physics, Zhejiang University, Hangzhou 310058, China

(Received 20 March 2024; accepted manuscript online 11 June 2024)

Fractional orbital angular momentum (OAM) vortex beams present a promising way to increase the data throughput in optical communication systems. Nevertheless, high-precision recognition of fractional OAM with different propagation distances remains a significant challenge. We develop a convolutional neural network (CNN) method to realize high-resolution recognition of OAM modalities, leveraging asymmetric Bessel beams imbued with fractional OAM. Experimental results prove that our method achieves a recognition accuracy exceeding 94.3% for OAM modes, with an interval of 0.05, and maintains a high recognition accuracy above 92% across varying propagation distances. The findings of our research will be poised to significantly contribute to the deployment of fractional OAM beams within the domain of optical communications.

DOI: 10.1088/0256-307X/41/7/074201

Since the seminal work by Allen *et al.* in 1992, which elucidated that optical vortex beams are capable of conveying orbital angular momentum (OAM),[1] the realm of optical OAM has attracted considerable attention across multiple disciplines, including optical communication,[2,3] optical tweezers,[4] optical imaging,[5] and quantum information processing.[6] Particularly within the sphere of optical communication, OAM is recognized for its substantial application prospects, attributed to its capacity to support an ostensibly infinite array of modes.[7–10] This characteristic of OAM beams opens up unprecedented opportunities for enhancing the bandwidth and efficiency of optical communication systems, thereby heralding a new era of high-capacity data transmission technologies.

Within these disciplines, the precise detection of OAM is a fundamental requisite for a lot of applications. Techniques employed for the quantification of OAM encompass interference patterns,[11] diffraction methodologies,[12] applications of cylindrical lenses,[13] and phase transformation strategies,[14,15] and so on. Notably, beams characterized by fractional OAM are capable of manifesting a more densely populated mode spectrum within identical spatial intervals compared to their integer OAM counterparts, thereby offering an enhanced channel capacity. Nonetheless, the subtleties inherent in fractional OAM beams necessitate more sophisticated recognition techniques,[16,17] particularly for applications demanding high-resolution discernment. In the landscape of traditional experimental research, a variety of methodologies have been devised to accurately measure fractional topological charges. These include the utilization of fork gratings,[18] the implementation of interferometer structures,[19,20] dynamic angular double slit experiments,[21] OAM sorting techniques,[22] the application of cylindrical lenses,[23] and the employment of multi-focus arrays.[24] Such methodologies facilitate the differentiation of OAM states with resolution parameters ranging from 0.1 to 0.3. This array of techniques underscores the progressive strides made towards refining the detection and measurement of fractional OAM, which is pivotal for harnessing the full potential of optical vortices in advanced optical systems.

In recent years, the advent of deep learning technology has profoundly revolutionized the domain of image recognition, providing new insights for the recognition of fractional OAM.[25–27] Commencing in 2019, Liu *et al.* pioneered the integration of deep learning methodologies for the explicit purpose of enhancing the precision in identifying fractional OAM.[28] This innovative approach marked the inception of a burgeoning research domain focused on the application of deep learning techniques to decipher fractional OAM across diverse scenarios. Notably, these scenarios encompass free-space optical communication,[29–31] mitigation of atmospheric turbulence effects,[32,33] and analyses of various fractional vortex beams.[34,35]

In the preceding investigations, applications of fractional OAM modes have met challenges of propagation instability. This instability has constrained the measurement of fractional OAM to predetermined distances, thereby introducing potential complications for communication endeavors. Acknowledging these limitations, our study introduces the deployment of an asymmetric Bessel (AB) beams imbued with fractional OAM. These beams are distinguished by their adjustable parameters, n and c, which facilitate the generation of OAM while demonstrating commendable propagation invariance. In our experiment, we utilize a spatial light modulator (SLM) equipped with amplitude holograms to engender the afore-

*Corresponding author. Email: dmz123@zju.edu.cn
© 2024 Chinese Physical Society and IOP Publishing Ltd

mentioned beams. This approach enables the creation of a dataset, comprising 20000 images, tailored for the investigation. To navigate the complexities of measuring fractional OAM across both fixed and variable distances, we adopt a convolutional neural network (CNN)-based architectural model.[36] This model has proven efficacious, achieving a recognition accuracy exceeding 90% with a precision of 0.05. Such achievements underscore the potential of integrating advanced optical configurations and deep learning methodologies for enhancing the robustness and versatility of optical communication systems, particularly in the context of utilizing fractional OAM modes.

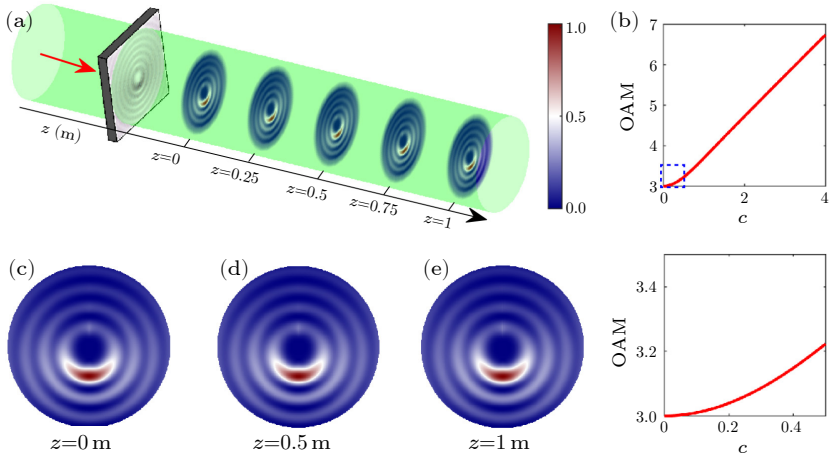

Fig. 1. Propagation characteristics and OAM properties of AB beams. (a) The generation method and propagation diagram of the AB beams, with parameters set as $n = 3$ and $c = 1.1$. (b) Relationship between the OAM carried by the AB beam and the asymmetric parameter c, with n fixed at 3. (c)–(e) Intensity profiles of the AB beam at different propagation distances.

In this study, we introduce AB beams as the light source. By solving the Helmholtz equation

$$(\nabla^2 + k^2)E(x, y, z) = 0, \tag{1}$$

where E is the electric field amplitude and k is the wave number, we obtain the expression of AB beams in cylindrical coordinates (r, φ, z):[37]

$$E_n(r, \varphi, z = 0; c) = \left[\frac{\alpha r}{\alpha r - 2c\exp(i\varphi)}\right]^{n/2} \cdot J_n\{\sqrt{\alpha r[\alpha r - 2c\exp(i\varphi)]}\}\exp(in\varphi), \tag{2}$$

where α is a constant related to the size of the beams, c means a parameter related to the asymmetry of the beams, J_n denotes the nth order Bessel function, and n is the vortex topological charge. Figure 1(a) illustrates the propagation characteristics of AB beams, which is generated by loading amplitude hologram on SLM. The simulated results demonstrate the stable propagation characteristics of the AB beams. Cross-sectional views of the transmission process are depicted more clearly in Figs. 1(c)–1(e), showing that the AB beams maintain the same intensity distribution at different distances. These beams carry fractional OAM, and the OAM carried by a unit-energy photon can be expressed as[37]

$$\frac{J_z}{I} = n + \frac{cI_1(2c)}{I_0(2c)} = n + \sum_{p=0}^{\infty}\frac{c^{2p}p}{(p!)^2}\left[\sum_{p=0}^{\infty}\frac{c^{2p}}{(p!)^2}\right]^{-1}. \tag{3}$$

Typically, the vortex phase topological charge induces integer-order variations in OAM. However, as depicted in Fig. 1(b), the unique asymmetric parameter c of AB beams leads to a non-integer OAM change, and when c is large, the relationship between them is essentially linear. When c is small, as shown in the enlarged image, their relationship is nonlinear and the variation of OAM with c becomes slower. The pattern of the light spot also becomes increasingly asymmetric as c increases. This change is reflected in both the simulation and experimental results, as shown in the following.

In the experiment, we employed amplitude holography to generate AB beams, utilizing the following Burch's encoding method:[38]

$$h(x, y) = 0.5\{1 + A^*(x, y)\cos[2\pi\rho x - \phi(x, y)]\}, \tag{4}$$

where $A(x, y)$ is normalized amplitude, $\phi(x, y)$ represents the phases of the object wavefront, and ρ is a constant.

The experimental setup is depicted in Fig. 2(a). A semiconductor laser with a central wavelength of 532 nm was utilized to generate a stable Gaussian beam. Polarizers and polarization beam splitters were then used to control the intensity and polarization of the beam. A telescope system expanded the light source, projecting it onto an SLM carrying an amplitude hologram. The intensity-type SLM used had a resolution of 1920×1080 pixels with an 8 μm pixel pitch. Subsequently, the beam passes through a $4f$ system to form the source field beam. After transmission, it is ultimately projected onto a complementary metal-oxide-semiconductor (CMOS) camera. Initially fixing the parameter n to 2 and 3, we progressively adjusted c from 0 to 2, with a resolution set at 0.01, to obtain beams with different fractional OAMs. By preprocessing the intensity images acquired by the camera, we generated a dataset, and subsequently input it into the neural network model we constructed for training.

The neural network we constructed is based on CNN (see details in the Supplementary Material), and the loss

function is average categorical cross-entropy:

$$L = -\frac{1}{N}\sum_{i=1}^{N}\sum_{j=1}^{M} y_{ij}\log(p_{ij}), \tag{5}$$

where N means the number of images, M is the number of categories for orbital angular momentum classification, y_{ij} represents the true orbital angular momentum of image i as j, and p_{ij} is the predicted probability of image i having orbital angular momentum j. This CNN-based framework embodies a sophisticated and robust approach to optical mode recognition, enabling the precise recognition of fractional-order OAM modes from intensity images. By leveraging advanced convolutional and pooling strategies, our model is poised to make significant contributions to the field of optical communications, enhancing the accuracy and reliability of OAM-based systems.

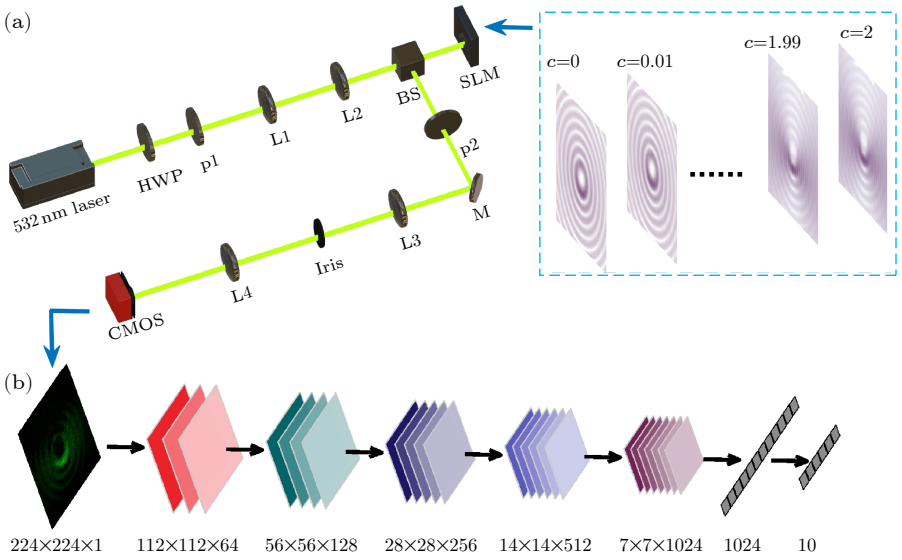

Fig. 2. The methodology employed for the detection of OAM in AB beams. (a) Generation of AB beams in the experiment, incorporating a half-wave plate (HWP), polarizers denoted as p1 and p2, a series of lenses labeled L1–L4, a beam splitter (BS), mirrors (M), culminating in the capture of images by a CMOS camera. (b) Structure of the neural network. Network input is a single channel map, and the subsequent output is a series of data blocks, which consist of feature maps. Convolution, MaxPooling, and ReLU operations are performed between each data block, a fully connected layer is employed for 10-class detection the feature maps.

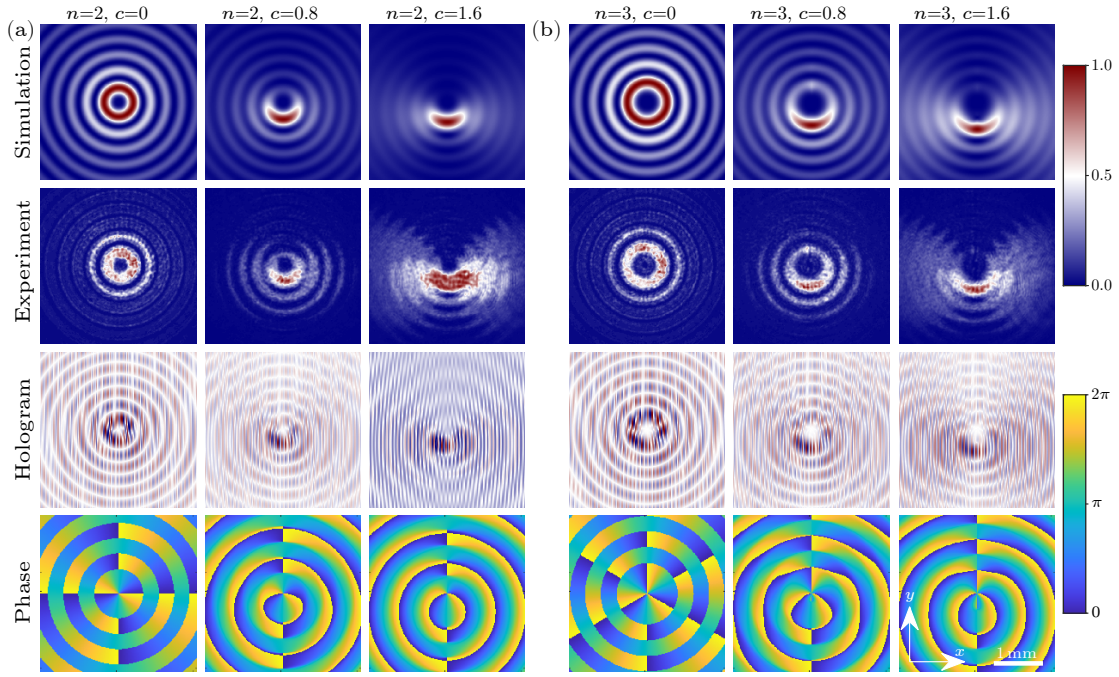

Fig. 3. The simulated and experimental results of the intensity and phase distribution of AB beams with different parameters. (a) The simulated and experimental results for various c with $n = 2$. (b) The simulated and experimental results for various c with $n = 3$.

In the conducted experiment, intensity distributions under varying parameter values of n and c are captured by CMOS. These parameters play a pivotal role in defining the characteristics of the AB beams. Figure 3 shows simulated and experimental results of the AB beam's intensity distribution characteristics alongside the corresponding phase and amplitude holograms for special values of n and c. The high consistency of the experimental and simulated results provides the data basis for the subsequent model training. When the parameter c is greater than 0, the asymmetry inherent in the AB beams becomes more evident, demonstrating the beam's deviation from symmetry with increasing c. Furthermore, the third row of Fig. 3 showcases the amplitude holograms loaded onto an amplitude-only SLM. The majority of the background coloration appears close to white, indicative of normalized intensity values approximating 0.5. This phenomenon arises from the nature of Burch's encoding method. Additionally, the fourth row of Fig. 3 shows the OAM characteristics of AB beams. Specifically, the light field's phase distribution adopts a helical configuration, punctuated by phase singularities at its nucleus at $c = 0$. When c is greater than 0, multiple phase singularities distributed along the y-axis are depicted in the phase plots on both sides of the x-axis. These phase singularities correspond to the dark regions observed in the intensity plots.

It is difficult for the human eyes to discern the differences between adjacent modes (see Fig. S1 in the Supplementary Material). In contrast, the deep learning approach not only automatically identifies different modes but also exhibits exceptionally high recognition accuracy. It is noted that AB beams differ from traditional fractional-order vortex beams. The hallmark non-diffracting property of the AB beams ensures that the optical field retains its structural integrity across varying distances. The feature significantly enhances the efficacy of machine learning algorithms in recognizing OAM modes irrespective of the transmission range. This capability partially addresses a critical challenge often encountered in optical communications and beam analysis, where distance-induced distortions can impede accurate mode recognition.

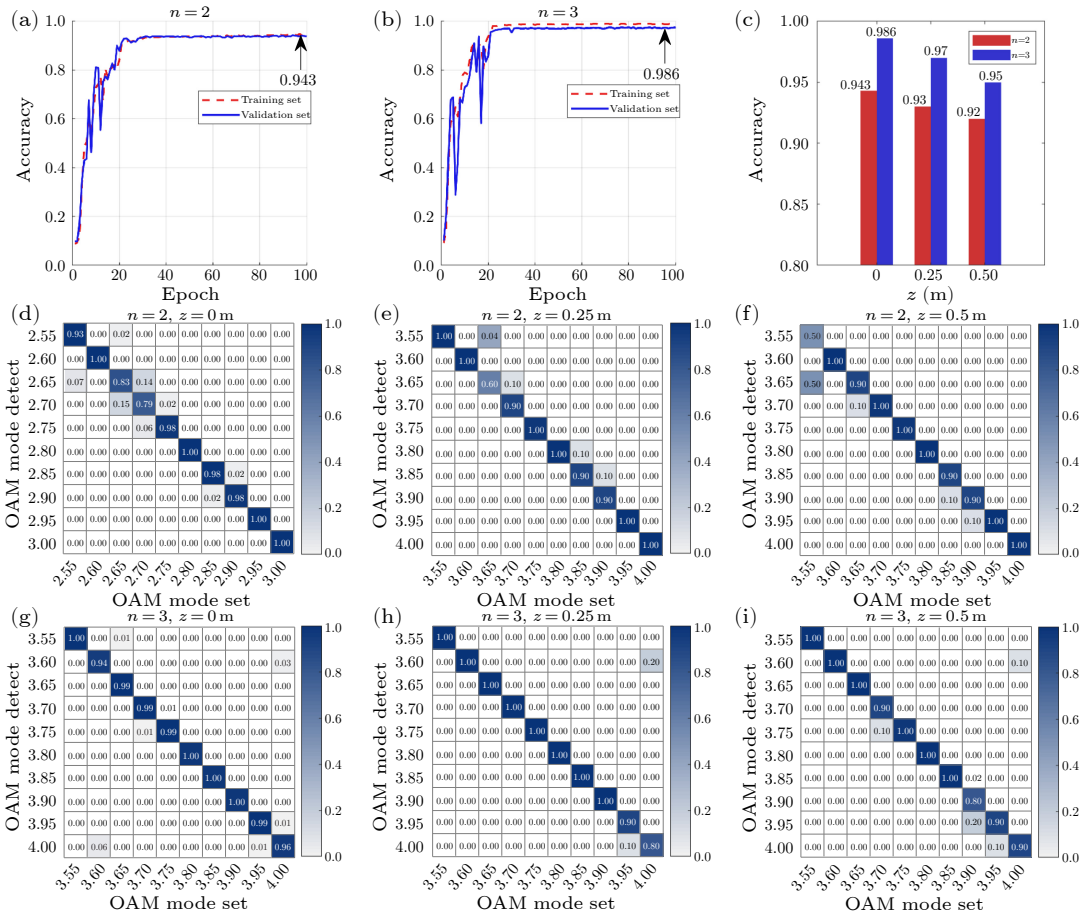

Fig. 4. Confusion matrices and accuracy of OAM recognition. [(a), (b)] Accuracy curves on the training and validation sets when $n = 2$ and $n = 3$, respectively. (c) The OAM detection accuracy at different transmission distances. (d)–(i) The confusion matrices of OAM detection at different transmission distances.

The pre-trained experimental intensity maps are employed for network training (see details in Supplementary Material). After training, we crafted a highly robust model that can recognize the OAM of AB beams with an interval of 0.05. Our model demonstrates an impressive recognition accuracy of 94.3% at $n = 2$, and an even more remarkable 98.6% at $n = 3$, exhibiting robustness under rotation and translation. The effectiveness of the model has been thor-

oughly validated, thus confirming the feasibility of deep learning methods for detecting fractional-order OAM in AB beam configurations.

The detailed performance dynamics of the model are presented in Figs. 4(a) and 4(b), which depict the evolution of recognition accuracy across both training and testing datasets over successive epochs. A characteristic pattern emerges from these visualizations: an initial phase of rapid accuracy fluctuations followed by a gradual ascent to a state of convergence, typically achieved within 20 epochs. For $n = 2$, the model represents an accuracy of 96% on the training set and an accuracy of 94.3% on the validation set. For $n = 3$, the model showcases an even more commendable accuracy of 99.1% on the training set and an accuracy of 98.6% on the validation set. These results demonstrate the model represents superior performance in OAM recognition.

The granularity of the model's performance is further revealed in the confusion matrices presented in Figs. 4(d) and 4(g). Through the testing of 1000 OAM mode images, each characterized by 0.05 intervals, for both $n = 2$ and $n = 3$, we observe the robust correspondence between the detected and the preset OAM modes. This discovery not only corroborates the deep learning model's capacity to pinpoint fractional OAM modes with high fidelity, but also showcases the potential of CNN-based frameworks in revolutionizing the analysis and application of complex optical phenomena.

For further experiments, we deployed 100 test images to assess the model's performance at two transmission distances ($z = 0.25\,\mathrm{m}$ and $z = 0.5\,\mathrm{m}$) to test the robustness of our model. Figure 4(c) shows a slight decrement in recognition accuracy as the transmission distance increases. The model's performance remains commendably high, with accuracy rates consistently exceeding 90%. This slight reduction in accuracy with distance is expected, but it underscores the elasticity of the model and the stable propagation properties of the AB mode. Figures 4(d)–4(i) display model's precision through the confusion matrices, which offer a granular view of the recognition accuracy with different distances. These matrices demonstrate our model's capacity to discern fractional-order OAM modes with high fidelity, even the transmission distance changes.

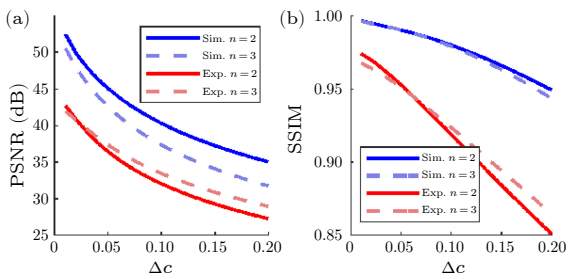

Fig. 5. Average PSNR and SSIM between adjacent modes under different precision requirements (Δc).

In our quest to refine the precision of OAM mode recognition through deep learning, we embark on a rigorous training regimen, tailoring it to accommodate various precision thresholds. This meticulous approach unveiled a direct correlation between the interval of adjacent OAM modes and the recognition accuracy achieved by the deep learning model. A pivotal observation emerged: as the interval between adjacent OAM modes was augmented to surpass 0.05, the model's recognition accuracy experienced a marked improvement, effortlessly attaining levels beyond 99.9% when the interval reached 0.1, which surpasses the error rate requirements of all current error correction techniques in communication systems. This enhancement underscores the model's adeptness in distinguishing between more distinctly spaced modes, leveraging the increased differentiation to bolster accuracy.

To gain deeper insights into this phenomenon, we delve into analyzing the impact of varying adjacent intervals (Δc) on two image quality metrics: the peak signal-to-noise ratio (PSNR) and the structural similarity index measure (SSIM).[39] PSNR and SSIM serve as benchmarks for evaluating the fidelity and perceptual quality of images under simulated and experimental conditions. PSNR provides a measure of the maximum error between adjacent OAM mode images, while SSIM assesses the visual impact of changes in structural information, brightness, and contrast:

$$\mathrm{PSNR} = 10 \times \log_{10}\left(\frac{\mathrm{MAX}^2}{\mathrm{MSE}}\right), \tag{6}$$

$$\mathrm{MSE} = \frac{1}{mn}\sum_{i=0}^{m-1}\sum_{j=0}^{n-1}[I_\mathrm{c}(i,\,j) - I_\mathrm{d}(i,\,j)]^2, \tag{7}$$

$$\mathrm{SSIM}(c,\,d) = \frac{(2\mu_\mathrm{c}\mu_\mathrm{d} + C_1)(2\sigma_\mathrm{cd} + C_2)}{(\mu_\mathrm{c}^2 + \mu_\mathrm{d}^2 + C_1)(\sigma_\mathrm{c}^2 + \sigma_\mathrm{d}^2 + C_2)}, \tag{8}$$

where MAX represents the maximum possible value of pixel intensity. MSE stands for mean squared error, $I_\mathrm{c}(i,\,j)$ and $I_\mathrm{d}(i,\,j)$ denote the pixel values at position $(i,\,j)$ in the images of the target mode and neighboring mode (where the adjacent interval is Δc), respectively, with m and n being the height and width of the images. Additionally, μ_c and μ_d represent the mean values of I_c and I_d, while σ_c and σ_d represent the variances of I_c and I_d, respectively; σ_cd indicates the covariance between I_c and I_d. Constants C_1 and C_2 are utilized to stabilize the calculation process.

The average changes in PSNR and SSIM are depicted in Fig. 5. When the Δc value is small, both the simulated and experimental image PSNR and SSIM are very high. Particularly, when Δc is less than 0.05, the PSNR of simulated images reaches over 45 dB, and SSIM exceeds 0.99, indicating extremely high similarity or low distinctiveness. This outcome results from the difficulties associated with pursuing high OAM accuracy (small Δc) and the characteristics of non-diffracting beams. As Δc exceeds 0.05, PSNR and SSIM rapidly decrease, suggesting easier recognition and higher accuracy. For experimental results, the PSNR and SSIM of images are relatively lower compared to simulations due to interference and noise inherent in the experiment. This does not imply better discrimination; instead, additional interference and noise lead to lower signal-to-noise ratios, posing more challenges for accurate recognition. To further improve recognition accuracy, we believe that increasing the pixel count of the images used for recognition (which also increases computational requirements), reducing noise in experiments, and

exploring more suitable network architectures would provide slight assistance.

In conclusion, we introduce non-diffracting AB beams endowed with fractional OAM, and the experimental results demonstrate the efficacy of a CNN-based deep learning approach in precisely identifying the fractional OAM imparted by such beams across varying distances. Despite the minimal differences between adjacent modes, as evidenced by exceedingly high PSNR and SSIM, and the presence of experimental noise, it is realized that our neural network models, tailored for $n = 2$ and $n = 3$, have achieved OAM mode recognition accuracies of 94.3% and 98.6%, respectively, with a precision of 0.05. Furthermore, the model's recognition capabilities extend beyond mere accuracy; the models demonstrate significant resilience, maintaining stable recognition performance amidst beam rotation and translation. Importantly, it consistently achieves recognition accuracies above 90% at different transmission distances. Our research proves the potential of integrating non-diffracting beams containing OAM with deep learning methodologies for optical communication and information processing applications, contributing valuable insights and tools to the field.

Acknowledgement. This work was supported by the National Natural Science Foundation of China (Grant Nos. 12174338 and 11874321).

References

[1] Allen L, Beijersbergen M W, Spreeuw R J C, and Woerdman J P 1992 *Phys. Rev. A* **45** 8185
[2] Padgett M J 2017 *Opt. Express* **25** 11265
[3] Wang J 2016 *Photon. Res.* **4** B14
[4] Skelton S E, Sergides M, Saija R, Iatì M A, Maragó O M, and Jones P H 2013 *Opt. Lett.* **38** 28
[5] Jack B, Leach J, Romero J, Franke-Arnold S, Ritsch-Marte M, Barnett S M, and Padgett M J 2009 *Phys. Rev. Lett.* **103** 083602
[6] Ndagano B, Nape I, Cox M A, Rosales-Guzman C, and Forbes A 2018 *J. Lightwave Technol.* **36** 292
[7] Wang J, Yang J Y, Fazal I M, Ahmed N, Yan Y, Huang H, Ren Y X, Yue Y, Dolinar S, Tur M, and Willner A E 2012 *Nat. Photon.* **6** 488
[8] Bozinovic N, Yue Y, Ren Y, Tur M, Kristensen P, Huang H, Willner A E, and Ramachandran S 2013 *Science* **340** 1545
[9] Gibson G, Courtial J, Padgett M J, Vasnetsov M, Pas'ko V, Barnett S M, and Franke-Arnold S 2004 *Opt. Express* **12** 5448
[10] Čelechovský R and Bouchal Z 2007 *New J. Phys.* **9** 328
[11] Leach J, Courtial J, Skeldon K, Barnett S M, Franke-Arnold S, and Padgett M J 2004 *Phys. Rev. Lett.* **92** 013601
[12] Hickmann J M, Fonseca E J S, Soares W C, and Chávez-Cerda S 2010 *Phys. Rev. Lett.* **105** 053904
[13] Peng Y, Gan X T, Ju P, Wang Y D, and Zhao J L 2015 *Chin. Phys. Lett.* **32** 024201
[14] Shen D and Zhao D 2019 *Opt. Lett.* **44** 2334
[15] Zhou X, Pang Z, and Zhao D 2022 *Ann. Phys.* **534** 2100471
[16] Leach J, Yao E, and Padgett M J 2004 *New J. Phys.* **6** 71
[17] Tao S H, Lee W M, and Yuan X C 2004 *Appl. Opt.* **43** 122
[18] Zhang N, Davis J A, Moreno I, Lin J, Moh K J, Cottrell D M, and Yuan X C 2010 *Appl. Opt.* **49** 2456
[19] Huang H C, Lin Y T, and Shih M F 2012 *Opt. Commun.* **285** 383
[20] Li P, Wang B, Song X, and Zhang X 2016 *Opt. Lett.* **41** 1574
[21] Zhu J, Zhang P, Fu D, Chen D, Liu R, Zhou Y, Gao H, and Li F 2016 *Photon. Res.* **4** 187
[22] Berger B, Kahlert M, Schmidt D, and Assmann M 2018 *Opt. Express* **26** 32248
[23] Alperin S N, Niederriter R D, Gopinath J T, and Siemens M E 2016 *Opt. Lett.* **41** 5019
[24] Deng D, Lin M, Li Y, and Zhao H 2019 *Phys. Rev. Appl.* **12** 014048
[25] LeCun Y, Bengio Y, and Hinton G 2015 *Nature* **521** 436
[26] Tong X, Xu R, Liu K, Zhao L, Zhu W, and Zhao D 2023 *Adv. Photon. Res.* **4** 2200264
[27] Tong X, Xu R, Xu P, Zeng Z, Liu S, and Zhao D 2023 *Adv. Photon.* **5** 066003
[28] Liu Z, Yan S, Liu H, and Chen X 2019 *Phys. Rev. Lett.* **123** 183902
[29] Na Y and Ko D K 2021 *Sci. Rep.* **11** 2678
[30] Cao F and Xie C 2022 *Appl. Opt.* **61** 4518
[31] Sun J J, Sun S, and Yang L J 2022 *IEEE Trans. Antennas Propag.* **70** 6775
[32] Cao M, Yin Y, Zhou J, Tang J, Cao L, Xia Y, and Yin J 2021 *Appl. Phys. Lett.* **119** 141103
[33] Zhou J, Yin Y, Tang J, Ling C, Cao M, Cao L, Liu G, Yin J, and Xia Y 2022 *Phys. Rev. A* **106** 013519
[34] Cao F, Pu T, and Xie C 2021 *Appl. Opt.* **60** 11134
[35] Wang H, Zhan Z, Shen Y, Hu J, Fu X, and Liu Q 2022 *Opt. Express* **30** 29781
[36] Zhu Y and Newsam S 2017 *IEEE International Conference on Image Processing (ICIP)*, Beijing, China, 17–20 September 2017, pp 790–794
[37] Kotlyar V V, Kovalev A A, and Soifer V A 2014 *Opt. Lett.* **39** 2395
[38] He L Q, Bai X L, and Lin J C 2012 *Inf. Technol. Appl. Industry* **263–266** 1568
[39] Lin W S and Jay Kuo C C 2011 *J. Vis. Commun. Image Represent.* **22** 297